

Hinge states in a system of coupled Rashba layers

Kirill Plekhanov , Flavio Ronetti, Daniel Loss , and Jelena Klinovaja

Department of Physics, University of Basel, Klingelbergstrasse 82, CH-4056 Basel, Switzerland



(Received 14 October 2019; published 27 January 2020)

We consider a system of stacked tunnel-coupled two-dimensional electron- and hole-gas layers with Rashba spin-orbit interaction subjected to a staggered Zeeman field. The interplay of different intralayer tunnel couplings results in a topological insulator phase characterized by the presence of gapless helical surface states. The staggered Zeeman field further enriches the topological phase diagram by generating a second-order topological insulator phase characterized by the presence of gapless hinge states. The emergence of these topological phases is proven analytically in the regime of small Zeeman field and confirmed by numerical simulations in the nonperturbative region of the phase diagram. The topological phases are stable against external perturbations and disorder.

DOI: [10.1103/PhysRevResearch.2.013083](https://doi.org/10.1103/PhysRevResearch.2.013083)

I. INTRODUCTION

Over the last decade, topological insulators and superconductors (TIs) have attracted a lot of attention in the domain of condensed matter physics [1–5]. One of the main reasons for such popularity resides in the bulk-boundary correspondence relating the topological description of a d -dimensional insulating bulk to the presence of gapless modes on a $(d - 1)$ -dimensional boundary of TIs. Moreover, the topological nature of the boundary modes makes them insensitive to a wide spectrum of external perturbations and disorder—the property of greatest importance in the area of quantum information and quantum computing [6–8]. Recently, the concept of bulk-boundary correspondence has been generalized by introducing a new class of topological systems, called higher-order TIs [9–13]. In contrast to conventional TIs, the $(d - 1)$ -dimensional boundary of an n th order TI is insulating, similarly to the bulk. Instead, it exhibits protected gapless modes on the $(d - n)$ -dimensional boundaries. The corresponding gapless modes are called corner states in the case $d \geq 2$, $n = d$ or hinge states for $d = 3$ and $n = 2$.

Following the pioneering works on higher-order TIs, great progress has been made in understanding these states of matter [14–33]. In two dimensions, the second-order TIs hosting corner states have been realized experimentally using electromagnetic circuits [34,35], photonic lattices [36,37], and waveguides [38], as well as phononic [39] and acoustic [40] setups. In three dimensions, there are strong indications that certain materials, such as SnTe [41] and bismuth [42], behave as second-order TIs hosting hinge states. However, only a few experimental realizations of higher-order TIs with a high level of control over the system parameters exist in $d \geq 3$ [43,44].

Motivated by this context, we propose here a mesoscopic setup that can be controllably brought into the second-order TI (SOTI) phase in three dimensions. The key component of our setup is an array of two-dimensional electron gas (2DEG) layers with Rashba spin-orbit interaction (SOI) and electron/holelike dispersions [45,46] (see Fig. 1). Different Rashba layers are tunnel coupled to each other, and the whole heterostructure is subjected to a staggered Zeeman field. The phase diagram of the resulting model comprises a strong three-dimensional topological insulator (3DTI) phase at zero Zeeman field, which transforms into the SOTI phase when the Zeeman field is switched on. In this work, we do not include the effect of interactions, but we point out the possibility to create even more exotic fractional higher-order topological states in a version of our system that contains strong electron-electron interactions [45,46].

This work is organized as follows. First, in Sec. II, we introduce the model for coupled Rashba layers. Second, in Sec. III, we present the phase diagram of the model in the regime of vanishing staggered Zeeman field. We show that the system exhibits a phase transition from the topologically trivial phase to the 3DTI phase hosting gapless surface states. Next, in Sec. IV, we analyze the effect of a staggered Zeeman field. We show that it gaps out the surface states and leads to the emergence of the SOTI phase hosting gapless hinge states. We also calculate the phase diagram of the model and study the stability of the topological phases against disorder. Finally, in Sec. V, we propose two modifications of the setup, which could facilitate the experimental realization. In the first proposal, the staggered Zeeman field is generated only on the surface of the heterostructure, using an antiferromagnet with a bicollinear antiferromagnetic order or via magnetic impurities. In the second proposal, the pairs of the 2DEGs are replaced by thin TI films.

II. MODEL

We start by introducing a system of coupled Rashba 2DEG layers [45,46] placed in the xy plane (see Fig. 1). We assume

Published by the American Physical Society under the terms of the Creative Commons Attribution 4.0 International license. Further distribution of this work must maintain attribution to the author(s) and the published article's title, journal citation, and DOI.

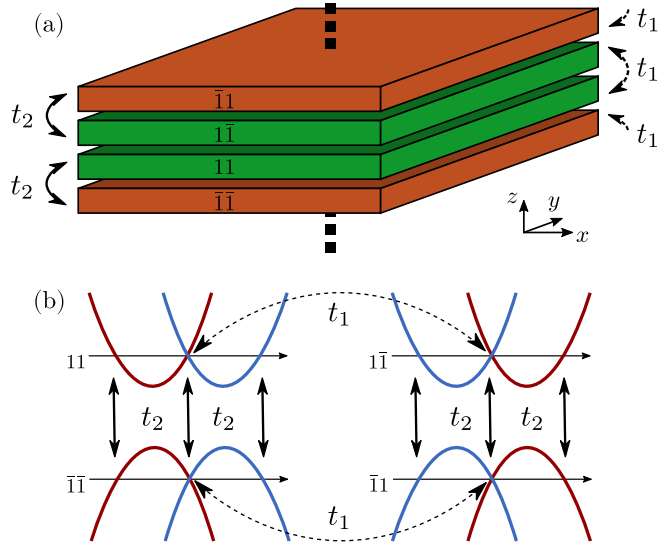


FIG. 1. (a) Schematic representation of the system of coupled Rashba layers. Different layers are characterized by different dispersion types, indexed by $\eta \in \{1, \bar{1}\}$, and different signs of the SOI amplitude, indexed by $\tau \in \{1, \bar{1}\}$. The layers of same (different) dispersion type (represented by the same color) are coupled via a t_1 (t_2) tunneling term. (b) A scheme showing different types of Rashba dispersions along the line $k_y = 0$ in momentum space. The tunneling process t_1 (t_2) coupling different Rashba layers is represented by dashed (solid) lines.

that the corresponding SOI vector is along the z axis and defines the spin quantization axis. The unit cell is composed of two pairs of layers with electron- and holelike dispersions described by opposite signs of the mass m and labeled by an index $\eta \in \{1, \bar{1}\}$. The layers of the same dispersion type are distinguished by the value of the SOI strength, which have the same amplitude α but opposite signs indexed by $\tau = \{1, \bar{1}\}$. Creation operators $\psi_{\eta\tau\sigma\mathbf{k}}^\dagger$ act on electrons with spin component σ along the z axis and momentum $\mathbf{k} = (k_x, k_y, k_z) \equiv (\mathbf{k}_\parallel, k_z)$ in the layer (η, τ) . Using this notation, the Hamiltonian describing the uncoupled layers reads

$$H_0 = \sum_{\eta\tau\sigma\sigma'} \int d^3k \psi_{\eta\tau\sigma\mathbf{k}}^\dagger [\mathcal{H}_{\eta\tau}^0(\mathbf{k})]_{\sigma\sigma'} \psi_{\eta\tau\sigma'\mathbf{k}}, \quad (1)$$

$$\mathcal{H}_{\eta\tau}^0(\mathbf{k}) = \left(\frac{\hbar^2 \mathbf{k}_\parallel^2}{2m} - \mu \right) \eta + \alpha \tau (\sigma_x k_y - \sigma_y k_x),$$

where the Pauli matrices σ_j act in spin space. The chemical potential μ is tuned to the crossing point of the spin-split bands at $\mathbf{k}_\parallel = 0$. In the following, it will be convenient to introduce the SOI energy $E_{\text{so}} = \hbar^2 k_{\text{so}}^2 / (2m)$ and the SOI momentum $k_{\text{so}} = m\alpha / \hbar^2$.

The nearest-neighbor Rashba layers are coupled to each other via spin-conserving tunneling processes. We distinguish two different types of tunnelings: between the layers with the same mass with the amplitude t_1 and between the layers with opposite masses with the amplitude t_2 . The corresponding processes are described by the following terms in the

Hamiltonian

$$H_1 = t_1 \sum_{\sigma} \int d^3k (\psi_{11\sigma\mathbf{k}}^\dagger \psi_{1\bar{1}\sigma\mathbf{k}} + e^{ik_z a} \psi_{1\bar{1}\sigma\mathbf{k}}^\dagger \psi_{11\sigma\mathbf{k}} + \text{H.c.}),$$

$$H_2 = t_2 \sum_{\sigma} \int d^3k (\psi_{11\sigma\mathbf{k}}^\dagger \psi_{\bar{1}\bar{1}\sigma\mathbf{k}} + \psi_{\bar{1}\bar{1}\sigma\mathbf{k}}^\dagger \psi_{11\sigma\mathbf{k}} + \text{H.c.}), \quad (2)$$

where a denotes the size of the unit cell in z direction.

Finally, the system is subjected to an effective Zeeman term

$$H_Z = t_Z \sum_{\eta\tau\sigma\sigma'} \eta \int d^3k \psi_{\eta\tau\sigma\mathbf{k}}^\dagger [\mathbf{n} \cdot \boldsymbol{\sigma}]_{\sigma\sigma'} \psi_{\eta\tau\sigma'\mathbf{k}}. \quad (3)$$

Here, $t_Z \eta n_j = \mu_B g_j B_j$, where \mathbf{B} is the magnetic field vector, \mathbf{n} is the direction of the Zeeman field, and g_j is the g factor along a given axis. We assume that the sign of the Zeeman splitting alternates between the Rashba layers with electron- and holelike dispersions. Such a staggered effective Zeeman field can be achieved in several ways. The first option is to use a uniform magnetic field and 2DEGs with opposite signs of the g factor in layers with different dispersions. A second possibility consists of using magnetic impurities which order ferromagnetically within the same Rashba layers but have a staggered magnetization direction in different layers [47–51]. Yet another option is to use thin ferromagnetically ordered layers, contained between the 2DEGs with the same dispersions. Alternatively, the effective Zeeman field can be applied only to the surface of the system, for example by placing it in the vicinity of a magnetic material, or by doping the surface with magnetic adatoms. As we will show later in Sec. V, these constructions allow us to reach the desired topological phases without affecting the bulk of the system.

After combining all previously introduced ingredients, the total Hamiltonian can be conveniently written in the basis $\Psi_{\mathbf{k}} = (\psi_{11\uparrow\mathbf{k}}, \psi_{11\downarrow\mathbf{k}}, \psi_{\bar{1}\bar{1}\uparrow\mathbf{k}}, \psi_{\bar{1}\bar{1}\downarrow\mathbf{k}}, \psi_{1\bar{1}\uparrow\mathbf{k}}, \psi_{1\bar{1}\downarrow\mathbf{k}}, \psi_{\bar{1}1\uparrow\mathbf{k}}, \psi_{\bar{1}1\downarrow\mathbf{k}})^T$ as

$$H = \int d^3k \Psi_{\mathbf{k}}^\dagger (\mathcal{H}_0 + \mathcal{H}_1 + \mathcal{H}_2 + \mathcal{H}_Z) \Psi_{\mathbf{k}},$$

$$\mathcal{H}_0 = \frac{\hbar^2 \mathbf{k}_\parallel^2}{2m} \eta_z + \alpha \tau_z (\sigma_x k_y - \sigma_y k_x),$$

$$\mathcal{H}_1 = t_1 \left(\frac{\eta_0 + \eta_z}{2} \tau_x + \frac{\eta_0 - \eta_z}{2} [\cos(k_z a) \tau_x - \sin(k_z a) \tau_y] \right),$$

$$\mathcal{H}_2 = t_2 \eta_x \tau_x, \quad \mathcal{H}_Z = t_Z \eta_z \mathbf{n} \cdot \boldsymbol{\sigma}, \quad (4)$$

where the Pauli matrices η_j and τ_j act in the space of four layers (η, τ) . In the following, we will present the solution of the problem described by the Hamiltonian H .

III. STRONG 3D TOPOLOGICAL INSULATOR

In order to describe the properties of our model, we first focus on the regime of vanishing Zeeman field ($t_Z = 0$). In this section, we calculate the topological phase diagram and deduce the effective degrees of freedom, associated with the topological surface states, emerging at low energies.

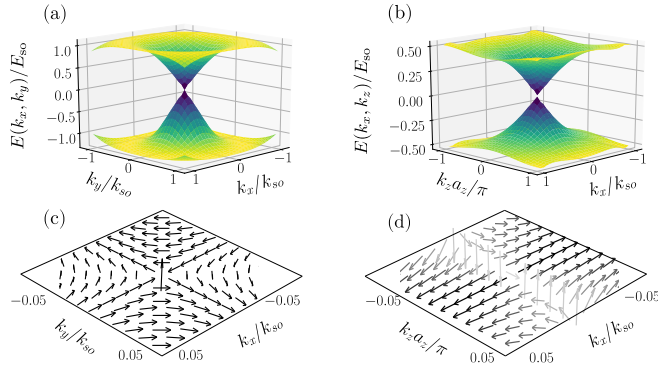


FIG. 2. Dirac cone dispersion relation of the surface states (a) $|\Phi_{\pm}^{xy}\rangle$ obtained in numerical simulations with PBC along the x and y axes and OBC along the z axis and (b) $|\Phi_{\pm}^{xz}\rangle$ obtained in numerical simulations with PBC along the x and z axis and OBC along the y axis. Both Dirac cones are centered at zero momentum. In (c), we show the spin polarization in momentum space of the states $|\Phi_{\pm}^{xy}\rangle$ in the surface layer at $z = 0$ and in (d) those of $|\Phi_{\pm}^{xz}\rangle$ in the surface layer at $y = 0$. The arrows represent the direction while the color intensity represents the absolute value of the spin-orbit polarization. Parameters of the simulations are $t_1 = 2t_2 = E_{so}$.

A. Topological phase diagram

When the Zeeman field is absent, the system is described by the Hamiltonian density

$$\mathcal{H}_{\text{TI}} = \mathcal{H}_0 + \mathcal{H}_1 + \mathcal{H}_2, \quad (5)$$

with the bulk spectrum given by

$$E^2(\mathbf{k}) = \epsilon^2 + (\alpha\mathbf{k}_{\parallel})^2 + t_1^2 + t_2^2 \pm 2\sqrt{\epsilon^2(\alpha\mathbf{k}_{\parallel})^2 + \epsilon^2 t_1^2 + t_1^2 t_2^2 \cos^2(k_z a/2)}, \quad (6)$$

where $\epsilon = \hbar^2 \mathbf{k}_{\parallel}^2 / (2m)$. The spectrum does not depend on the direction of the in-plane vector \mathbf{k}_{\parallel} as a consequence of the rotational symmetry in the xy plane. We also see that at zero momentum, $\mathbf{k} = 0$, the two tunneling processes compete with each other, leading to the closing of the gap at the critical point $t_1 = t_2$. As a result, the phase diagram is divided into two regimes: $t_1 < t_2$ and $t_1 > t_2$.

The Hamiltonian density satisfies the relation $T\mathcal{H}_{\text{TI}}(\mathbf{k})T^{-1} = \mathcal{H}_{\text{TI}}(-\mathbf{k})$, implying that the system is time-reversal symmetric. Here the time-reversal symmetry operator is expressed as $T = i\sigma_y K$, with K being the complex conjugation operator. However, we note that the particle-hole symmetry and the chiral symmetry are absent. Hence, the system belongs to the AII symmetry class characterized by a topological invariant $\nu_0 \in \mathbb{Z}_2$ (see Appendix C 1 for more details). The bulk-boundary correspondence relates this topological invariant to the presence of gapless states $|\Phi_{\pm}^s\rangle$ localized at every surface s of the system and decaying exponentially into the bulk. We verify numerically the presence of such gapless surface states in the regime $t_1 < t_2$ of our model by diagonalizing the discretized version of the Hamiltonian \mathcal{H}_{TI} density, as shown in Figs. 2(a) and 2(b). This allows us to identify the regime $t_1 < t_2$ ($t_1 > t_2$) with the topologically trivial (topological) phase, where the topological phase corresponds to a strong 3DTI [45,46].

We study the surface states more closely by considering several nonequivalent geometries of the system with open boundary conditions (OBCs) along one direction and periodic boundary conditions (PBCs) along two other directions. In particular, we study the xy surface states in a geometry with OBC along the z axis and PBCs along the x and y axes [see Fig. 2(a)], and the xz surface in a geometry with OBC along the y axis and PBCs along the x and z axis [see Fig. 2(b)]. We observe that the surface states have a linear dispersion relation with one Dirac cone per surface. The shape of the Dirac cone and the spin texture of the surface states change depending on the surface considered. As a consequence of the rotational symmetry in the xy plane, the Dirac cone on the xy surface is isotropic, and the spin texture is antivortexlike [see Fig. 2(c)]. With our choice of the spin quantization axis along the z axis, the spin polarization of the surface states $|\Phi_{\pm}^{xy}\rangle$ lie in the xy plane. In contrast, the Dirac cone on the xz surface is tilted. Moreover, the spin texture of the states $|\Phi_{\pm}^{xz}\rangle$ is dominated by the x component of the spin polarization [see Fig. 2(d)] almost everywhere except on the line $k_x = 0$, where the polarization along the z axis becomes dominant.

B. Gapless surface states

In order to acquire a better understanding of the 3DTI phase, we demonstrate the emergence of gapless surface states explicitly by finding the wave functions of their states $|\Phi_{\pm}^s\rangle$ located at different surfaces s . The details of these calculations are given in Appendix A. For clarity, we only focus on the solutions at the Dirac point, which are obtained by taking two of three components of the momentum \mathbf{k} to zero. Later, the terms linear in momentum are treated perturbatively, giving us the information about the effective low energy Hamiltonian of surface states close to the Dirac point.

1. Top and bottom surfaces

First, we focus on the xy surface by taking $\mathbf{k}_{\parallel} = 0$. We rewrite the problem in a geometry with OBC along the z axis by substituting $k_z \rightarrow -i\partial_z$. We assume that the linear size L_z of the system in the z direction is sufficiently large such that the surface states at opposite surfaces can be treated as independent. The resulting simplified real-space Hamiltonian density reads

$$\mathcal{H}_{\text{TI}}^{xy} = t_2 \eta_x \tau_x + t_1 \tau_x + it_1 a \partial_z \frac{\eta_0 - \eta_z}{2} \tau_y. \quad (7)$$

Here, we only consider the terms linear in momentum k_z . We note that, in addition to a time-reversal symmetry T already present in the full problem, the simplified Hamiltonian has a particle-hole symmetry represented by an operator $P = -\tau_z K$ satisfying $P\mathcal{H}_{\text{TI}}^{xy}P^{-1} = -\mathcal{H}_{\text{TI}}^{xy}$ and $[P, T] = 0$. Moreover, the chiral symmetry described by an operator $C = TP = -i\tau_z \sigma_y$ is also present in the system. Enforced by these symmetries, the Dirac point of the surface states is located exactly at zero energy.

The dispersion relation and the effective Hamiltonian at small finite momentum \mathbf{k}_{\parallel} is obtained perturbatively by calculating the expectation values of the remaining terms in \mathcal{H}_{TI} in the basis of the surface states $|\Phi_{\pm}^{xy}\rangle$. This allows us to write the effective low-energy Hamiltonian density of the top

xy surface as

$$\mathcal{H}_{\text{TI}}^{\text{xy}}(z=0) \approx \alpha(\rho_x k_y - \rho_y k_x)(t_1 - t_2)/\bar{t}, \quad (8)$$

where ρ_j act in the space of the surface states $|\Phi_{\pm}^{\text{xy}}\rangle$ and where we took into account only the terms linear in k_x and k_y , see Appendix A for details. We recover the Dirac cone dispersion relation of the surface states and note that at finite momentum $k_{\parallel} \neq 0$ the spin polarization is momentum-locked. Combined with the rotational symmetry in the xy plane, this results in the antivortexlike spin texture observed numerically in Fig. 2(c).

The low-energy description of the bottom xy surface can be derived by making use of the symmetry transformation $z \rightarrow L_z - z$, $\mathbf{e}_j \rightarrow -\mathbf{e}_j$, where \mathbf{e}_j are three basis unit vectors. Indeed, one finds that the low-energy Hamiltonian of bottom and top xy surfaces are the same

$$\mathcal{H}_{\text{TI}}^{\text{xy}}(z=L_z) = \mathcal{H}_{\text{TI}}^{\text{xy}}(z=0). \quad (9)$$

2. Lateral surfaces

In the same way as for the top and bottom surfaces, we express the states $|\Phi_{\pm}^{\text{xz}}\rangle$ localized on the xz surface in the neighborhood of the Dirac point, by considering $(k_x, k_z) = 0$ and making the substitution $k_y \rightarrow -i\partial_y$. We also assume that the linear size L_y of the system in the y direction is sufficiently large such that the exponentially small overlap between the states at opposite surfaces can be neglected. The corresponding problem reads

$$\mathcal{H}_{\text{TI}}^{\text{xz}} = -\frac{\hbar^2 \partial_y^2}{2m} \eta_z - i\alpha \partial_y \tau_z \sigma_x + t_2 \eta_x \tau_x + t_1 \tau_x. \quad (10)$$

We note that the simplified Hamiltonian density has a new particle-hole symmetry $P = \eta_x \tau_z K$ and a new chiral symmetry $C = i\eta_x \tau_z \sigma_y$, which both commute with T . As a consequence, the lateral surface states also have to be at zero energy and satisfy $T|\Phi_{\pm}^{\text{xz}}\rangle = \pm|\Phi_{\mp}^{\text{xz}}\rangle$ and $P|\Phi_{\pm}^{\text{xz}}\rangle = |\Phi_{\pm}^{\text{xz}}\rangle$. As a result, the effective low-energy Hamiltonian of the surface states at $y=0$ can be written as

$$\mathcal{H}_{\text{TI}}^{\text{xz}}(y=0) \approx \alpha A k_x \rho_z + t_1 B k_z a \rho_x, \quad (11)$$

where ρ_j act in the space of the surface states $|\Phi_{\pm}^{\text{xz}}\rangle$ and where A and B are dimensionless constant that can be found numerically, see Appendix A for details. We recover the tilted Dirac cone dispersion relation observed in Fig. 2(d).

The effective Hamiltonian of the lateral surface at $y=L_y$ is obtained by using the transformation $y \rightarrow L_y - y$, $\mathbf{e}_j \rightarrow -\mathbf{e}_j$ that preserves the surface orientation such that the normal vector $\mathbf{v}_{\perp}^{\text{xz}}$ pointing outwards of the surface coincides with the vector \mathbf{e}_y . We find that the low-energy effective Hamiltonian density remains invariant under this transformation

$$\mathcal{H}_{\text{TI}}^{\text{xz}}(y=L_y) = \mathcal{H}_{\text{TI}}^{\text{xz}}(y=0). \quad (12)$$

Finally, the low-energy description of the two remaining yz surfaces can be obtained using the rotational symmetry in the xy plane described by the transformation $\{L_x - x, y\} \rightarrow \{y, x\}$. Under this transformation, the low-energy Hamiltonian describing the two yz surfaces becomes

$$\mathcal{H}_{\text{TI}}^{\text{yz}}(x=0) = \mathcal{H}_{\text{TI}}^{\text{yz}}(x=L_x) \approx -\alpha A k_y \rho_z + t_1 B k_z a \rho_x. \quad (13)$$

We see that the momentum component k_x is replaced by k_y , but the structure of the low-energy Hamiltonian remains invariant.

IV. SECOND-ORDER 3D TOPOLOGICAL INSULATOR

In this section, we describe the low-energy physics of our system under applied staggered Zeeman field ($t_z \neq 0$). For this purpose, we consider the full Hamiltonian density

$$\mathcal{H}_{\text{SOTI}} = \mathcal{H}_0 + \mathcal{H}_1 + \mathcal{H}_2 + \mathcal{H}_Z. \quad (14)$$

The crucial role of the Zeeman term \mathcal{H}_Z consists in gapping out the surface states $|\Phi_{\pm}^s\rangle$. As a result, the system ceases to be a 3DTI. Nevertheless, as we will explain below in this section, the topological description of the resulting system becomes even richer, supporting the emergence of chiral hinge states characteristic to three-dimensional SOTI. We also note that the spatial oscillation of the staggered Zeeman field in \mathcal{H}_Z is crucial to achieve our goal. More precisely, one can show that a uniform Zeeman field fails to gap out all the surface states, and does not lead to hinge states (see Appendix B for more details).

A. Small Zeeman field

In a first step, we consider the regime of a small staggered Zeeman field $t_z \ll t_1, t_2$. In this way, by treating the Zeeman field perturbatively, we demonstrate that the gap opens in the spectrum of the Dirac cones of surface states (see Appendix A 3 for details).

1. Top and bottom surfaces

The expression of the wave functions $\Phi_{\pm}^{\text{xy}}(z)$ of the surface states located on the xy surfaces, derived in Appendix A 1, can be used to project the Zeeman term \mathcal{H}_Z in the vicinity to the Dirac point. The resulting effective low-energy Hamiltonian density describing the xy surfaces of the 3DTI under the applied Zeeman field is given by

$$\begin{aligned} \mathcal{H}_{\text{SOTI}}^{\text{xy}}(z=0) &\approx \alpha(\rho_x k_y - \rho_y k_x)(t_1 - t_2)/\bar{t} \\ &\quad - M_{xy}(n_x \rho_x + n_y \rho_y - n_z \rho_z), \end{aligned} \quad (15)$$

$$\begin{aligned} \mathcal{H}_{\text{SOTI}}^{\text{xy}}(z=L_z) &\approx \alpha(\rho_x k_y - \rho_y k_x)(t_1 - t_2)/\bar{t} \\ &\quad + M_{xy}(n_x \rho_x + n_y \rho_y - n_z \rho_z), \end{aligned} \quad (16)$$

where $M_{xy} = t_z(t_1 + t_2)/\bar{t}$ is a ‘‘mass term’’ induced by the z component of the Zeeman field. The x and y components of the Zeeman field simply shift the position of the Dirac cone in momentum space. In contrast, the mass term anticommutes with all the remaining terms in $\mathcal{H}_{\text{SOTI}}^{\text{xy}}$ and gaps out the surface states $|\Phi_{\pm}^{\text{xy}}\rangle$. These analytical predictions are confirmed by a numerical diagonalization of $\mathcal{H}_{\text{SOTI}}$ presented in Fig. 3(a). Importantly, the expectation value of the Zeeman term in the basis of the surface states of the bottom surface is exactly opposite to the one of the top xy surface, leading to an inversion of the sign of the mass term between the two surfaces. In the following, we will show an important consequence of this result.

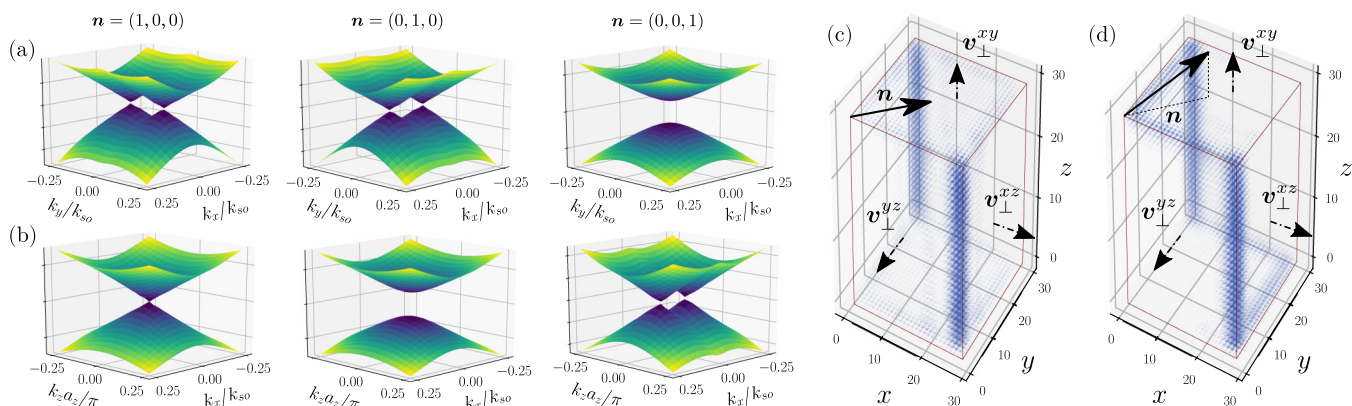


FIG. 3. The effect of the staggered Zeeman field on the dispersion relation of the surface states (a) $|\Phi_{\pm}^{xy}\rangle$ and (b) $|\Phi_{\pm}^{xz}\rangle$. The direction of the Zeeman field is indicated by the vector \mathbf{n} . While the Zeeman field parallel to the surface either shifts the Dirac cone or does not affect the energy dispersion of the surface states at all, the Zeeman field perpendicular to the surface opens a gap. Parameters of the simulations are $t_1 = 2t_2 = E_{so}$, $t_z = 0.3E_{so}$. [(c) and (d)] Probability density of the gapless hinge state obtained in numerical simulations with OBCs along the x , y , and z axes. The sign of the mass term generated by the Zeeman field is equal to the sign of $\mathbf{v}_{\perp}^s \cdot \mathbf{n}$, where \mathbf{v}_{\perp}^s is the outward-pointing unit vector perpendicular to the surface s . (c) If $\mathbf{n} = (1, 1, 0)/\sqrt{2}$, the Zeeman field opens a gap at the xz and yz surfaces but leaves the xy surface gapless. (d) If $\mathbf{n} = (1, 1, 1)/\sqrt{3}$, all the surfaces become gapped. In both cases, hinge states emerge at the interface between gapped surfaces with opposite signs of the mass M_s . Parameters of the simulations are $t_1 = 2t_2 = 4E_{so}$, $t_z = 2E_{so}$.

2. Lateral surfaces

The low-energy effective description of lateral surfaces in presence of the staggered magnetic field can be obtained by performing similar calculations, leading us to

$$\mathcal{H}_{\text{SOTI}}^{xz}(y=0) \approx \alpha A k_x \rho_z + t_1 B k_z a \rho_x + t_z C (n_y \rho_y + n_z \rho_z), \quad (17)$$

$$\mathcal{H}_{\text{SOTI}}^{xz}(y=L_y) \approx \alpha A k_x \rho_z + t_1 B k_z a \rho_x - t_z C (n_y \rho_y + n_z \rho_z). \quad (18)$$

Surprisingly, we find that the Zeeman field along the x direction does not have any effect on the surface states. The z component of the Zeeman field simply shifts the Dirac cone along the x axis in the momentum space, while the y component gaps out the surface states by inducing a mass term with the amplitude $M_{xz} = t_z C n_y$ (see Appendix A 3 for details). We confirm these analytical predictions by performing a numerical diagonalization of $\mathcal{H}_{\text{SOTI}}$ with the results being shown in Fig. 3(b).

Finally, the effective description of the two yz surfaces is obtained by using the rotational symmetry in the xy plane. We get

$$\mathcal{H}_{\text{SOTI}}^{yz}(x=0) \approx -\alpha A k_y \rho_z + t_1 B k_z a \rho_x + t_z C (n_x \rho_y + n_z \rho_z), \quad (19)$$

$$\mathcal{H}_{\text{SOTI}}^{yz}(x=L_x) \approx -\alpha A k_y \rho_z + t_1 B k_z a \rho_x - t_z C (n_x \rho_y + n_z \rho_z). \quad (20)$$

We note that the roles of the Zeeman field components along the x and y axes are interchanged. However, the mass term still gaps out the surface states and the sign of the mass term is opposite for the two surfaces.

B. Emergence of the hinge states

As we have seen previously, the effective low-energy description of the surface states $|\Phi_{\pm}^s\rangle$ of the 3DTI in the absence of the Zeeman field is characterized by the Dirac cone dispersion relation. The staggered Zeeman field opens a gap at the Dirac point by inducing a mass term with the amplitude M_s . The sign of M_s is equal to the projection of the Zeeman field vector \mathbf{n} onto the outward-pointing normal unit vector \mathbf{v}_{\perp}^s , which changes sign between opposite surfaces. Hence, if all the surfaces of the system are gapped, a set of gapless chiral modes has to emerge at the hinge interfaces that connect the surfaces with opposite signs of M_s . Such gapless chiral modes are denoted as hinge states. We use the existence of the hinge states as a criterion to identify the emergence of a SOTI topological phase.

An exact position of the hinge states is determined by calculating $\mathbf{v}_{\perp}^s \cdot \mathbf{n}$ on every surface. The presence of the hinge states is confirmed numerically by diagonalizing $\mathcal{H}_{\text{SOTI}}$ in a geometry with OBCs along all three directions shown in Figs. 3(c) and 3(d) where we consider two general non-collinear orientations of the Zeeman field. In Fig. 3(c), the Zeeman field is taken to be parallel to the xy surface, but making a finite angle with both the xz and yz surfaces. As a result, the two hinge states emerge at the interfaces ($x = L_x, y = 0$) and ($x = 0, y = L_y$) that connect the xz and yz surfaces with opposite signs of $\mathbf{v}_{\perp}^s \cdot \mathbf{n}$. The mass term on the xy surfaces is zero such that the whole surfaces remain gapless. In Fig. 3(d), the Zeeman field makes a finite angle with all three surfaces, gapping out the xy surface and leading to the emergence of four additional hinge states at ($x = L_x, z = 0$), ($y = L_y, z = 0$), ($x = 0, z = L_z$), and ($y = 0, z = L_z$). In both cases, the gapless chiral state separates the entire surface of the system into two regions with opposite values of the mass M_s .

Deforming the system geometry affects the exact position of the hinge state but does not remove it. In particular, the

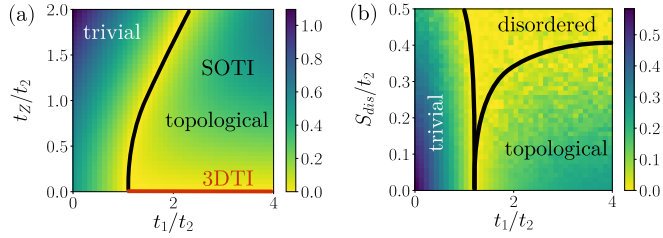


FIG. 4. (a) Topological phase diagram showing boundaries between different phases as well as the energy of the first excited state as a function of the ratios t_1/t_2 and t_z/t_2 for $t_2 = 0.5E_{so}$ (color coded in units of E_{so}). The 3DTI phase (represented by the red line) exists in the regime $t_1 > t_2$ in the absence of Zeeman field. The SOTI phase emerges from the 3DTI at finite values of t_z . A critical value of the ratio t_1/t_2 separating the SOTI topological phase and the trivial gapped phase (represented by the black line) increases with the strength of the Zeeman field. The position of this critical line is not affected by the direction of the Zeeman field. This diagram was obtained with periodic boundary conditions along the x and y axes and open boundary conditions along the z axis. (b) Topological phase diagram showing the stability of the topological phase against external perturbation and disorder as a function of the ratios t_1/t_2 and S_{dis}/t_2 , where $S_{dis} := S_\mu = S_z = S_\alpha$. Every point on the phase diagram corresponds to a unique realization of the disorder. We see that the topological phase is stable even for perturbations of the strength larger than the gap of the surface states. When the perturbations become stronger, the gap closes. The parameters of the simulation are $t_2 = 0.5E_{SO}$ and $t_z = 0.3E_{SO}$.

rectangular geometry considered above can be deformed into a sphere. Then, the Zeeman field will split the sphere into two symmetric semi-spheres with opposite signs of M_s , leading to the emergence of a gapless chiral mode at the equator. Such a behavior is related to the presence of the inversion symmetry with the symmetry operator $I = \tau_x$ satisfying $I\mathcal{H}_{SOTI}(\mathbf{k})I^{-1} = \mathcal{H}_{SOTI}(-\mathbf{k})$. The presence of the inversion symmetry also allows us to calculate the bulk topological invariant describing the SOTI phase (see Appendix C 2 for more details).

C. Phase diagram

Previously, we obtained a simple low-energy description of the model using the projection onto the space of surface states $|\Phi_\pm^s\rangle$. This description is valid only as long as $t_z \ll t_1, t_2$. A complete phase diagram, including the regime of strong staggered Zeeman field, is obtained numerically by calculating the gap to the first excited state as a function of the ratios t_1/t_2 and t_z/t_2 . The result of this calculation is shown in Fig. 4(a). There we see that the 3DTI phase is stable in the regime $t_1 > t_2$ at strictly zero t_z , characterized by the presence of a gapless surface. At finite values of t_z , the SOTI phase emerges from the 3DTI phase, leading to the appearance of a gap to the first excited state. Both 3DTI and SOTI phases are gapped in the bulk. We also clearly see the critical line which separates the trivial phase at strong t_2 and the topological phase at strong t_1 . The Zeeman field shifts the phase boundary so that higher values of the ratio t_1/t_2 are required to reach the SOTI phase. Along this critical line, the system is gapless in the bulk. The numerical calculations are performed for several directions of the Zeeman field vector \mathbf{n} but we find that it

hardly affects the position of the critical line despite the strong anisotropy present in the system.

Finally, we discuss the stability of our setup with respect to external perturbations and disorder. We verify numerically that the topological states are not affected by local on-site disorder such as a fluctuating chemical potential or a Zeeman field generated by magnetic impurities. In our calculations, the disorder is implemented using a uniform distribution with zero mean and standard deviations S_μ and S_z . Similarly, we check that the presence of topological phases is not affected by the offset of fine tuned parameters in different Rashba layers, such as the SOI amplitude α and the chemical potential μ . For this purpose, each Rashba layer is equipped with a set of two random variables, describing the offset of the SOI amplitude α and the chemical potential μ . The random variables are taken from a uniform distributions with standard deviations S_α and S_μ . These random variables are constant within each Rashba layer and only differ between different Rashba layers. The topological phase diagram showing different phases as well as the values of the gap to the first excited state in a disordered system is presented in Fig. 4(b). We find that even though the disorder breaks the inversion symmetry I and disallows the usage of the topological invariant of the SOTI phase, the hinge states are stable against the random perturbations of a strength of the order of the gap.

V. MODIFIED SETUPS

In this last section, we consider two alternative approaches to generate the topological phase hosting hinge modes, which could help to facilitate experimental realizations.

A. Magnetic proximity setup

From above considerations, we know that the staggered Zeeman field has an effect only on the surface as the 3D bulk modes are already gapped out by the tunneling between layers. Thus, we can consider a magnetic proximity setup where the staggered Zeeman field is induced only on the surface of the 3DTI and not in the bulk. Such a surface Zeeman field gaps out the states $|\Phi_\pm^s\rangle$ by locally breaking the time-reversal symmetry at the surface. It leads to the emergence of hinge states without affecting the bulk properties of the system. The effect of the surface Zeeman field is tested numerically by calculating the gap to the first excited surface state, as a function of the ratio t_z/t_2 and the penetration length of the Zeeman field l_z . The result of this calculation is shown in Fig. 5(a). We find that even a very small penetration length, of the order of a few unit cells, is enough to fully gap out the surface states. Moreover, we observe that the topological phase transition occurs as a function of the surface Zeeman field. The position of the phase transition is not affected by the value of the penetration length l_z and is independent of the bulk properties of the system.

An experimental realization of the staggered surface Zeeman field can be achieved by using magnetic adatoms [47–49] or by placing an antiferromagnetic material with a bicollinear antiferromagnetic ordering close to the Rashba layer heterostructure such that the size of the magnetic unit cell along

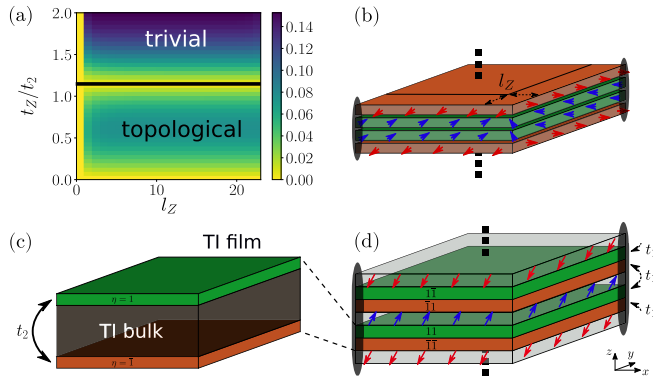


FIG. 5. (a) Topological phase diagram showing boundaries between different phases as well as the size of the energy of the first excited state as a function of the ratio t_z/t_2 and the penetration length of the Zeeman field l_z for $t_1 = 1.5t_2 = 0.75E_{so}$ (color coded in units of E_{so}). The surface states are completely gapped out even for a very small penetration length of the order of 2 unit cells. We note that the gap closes for $t_z \approx 1.1t_2$ (represented by the black line), indicating a topological phase transition. (b) Schematic representation of the Zeeman proximity setup in which a staggered Zeeman field (represented by red and blue arrows) is generated by proximity to an antiferromagnetic material or by depositing magnetic adatoms on the surface of the Rashba layer heterostructure. (c) A scheme representing a thin TI film (only top and bottom gapless surface modes are shown). Due to the finite width of the film gapless surface modes localized at the top and bottom surfaces are coupled via the t_2 term. (d) Schematics of a coupled-layer setup of thin TI films. Surface modes of neighboring TIs with different helicities (represented by different colors) are coupled to each other via a t_1 term. Ferromagnetic layers of opposite magnetization direction (red and blue arrows) are inserted between the TIs to generate a staggered Zeeman field. A pair of emerging hinge states is shown by two ellipsoids.

the z direction of the magnet matches the distance a , as shown in Fig. 5(b). The required antiferromagnetic materials, such as iron tellurium (FeTe), have been studied both theoretically [52] and experimentally [53]. Such materials have also been used experimentally in a proximity setup with Bi_2Se_3 [54]. This setup adds flexibility in controlling the value of the mass term M_s on different surfaces, which can be achieved by adjusting the position of the antiferromagnetic material or controlling the deposition of magnetic atoms. This allows one to shift the position of the hinge state or even generate several interfaces of zero M_s on a single 3DTI surface.

B. Coupled TI films

Second, we propose an alternative coupled-layer construction where the 2DEGs with opposite dispersions are substituted by thin three-dimensional TI films, such as $\text{Bi}_{1-x}\text{Sb}_x$ [55], Bi_2Te_3 [56], or TlBiSe_2 [57]. A thin TI film can be interpreted as a bilayer material hosting a pair of gapless surface states with the Dirac dispersion relation at opposite surfaces [see Fig. 5(c)]. The finite width of the TI induces a tunnel coupling between the surface states, mediated by the bulk modes of the TI. We identify such a coupling term with the tunneling term \mathcal{H}_2 in Eq. (4). Moreover, stacking several

TI films along the z direction leads to another tunnel coupling between the surface states localized in neighboring TIs, which we identify with the tunneling term \mathcal{H}_1 in Eq. (4).

Similarly to the coupled 2DEG layer system, the TI layer setup requires a staggered Zeeman field to gap out the lateral surfaces. The Zeeman field has to change sign from one surface of the TI film to another, and keep the same sign at the interface between different TIs. The simplest way to realize such a Zeeman field consists in using thin ferromagnetic layers contained between the TI films. Alternatively, the effective Zeeman field can be generated using magnetic impurities. The schematic representation of the TI layer setup subjected to a staggered Zeeman field is shown in Fig. 5(d).

VI. CONCLUSIONS

To summarize, in this work we considered a system of coupled Rashba layers subjected to a staggered Zeeman field. Such a model can be realized experimentally by using 2DEGs with opposite signs of the g -factor, by depositing magnetic adatoms, or by placing an antiferromagnet with a bicollinear antiferromagnetic order close to the system surface. A similar effective model can also be obtained by considering an array of coupled thin TI layers. At zero Zeeman field, the system experiences a topological phase transition from the trivial insulator to the strong 3DTI which hosts gapless modes at its surface. Focusing on the low-energy degrees of freedom associated with the surface states, we calculated perturbatively the effect of the Zeeman term. We found that it leads to the emergence of a mass term for gapless surface excitations that gaps them out. The amplitude of the mass term is determined by the direction of the Zeeman field and inevitably changes sign at opposite surfaces of the system. This leads to the emergence of zero-mass hinge interfaces hosting chiral gapless hinge states, characteristic for the SOTI phase. We confirmed numerically the presence of the hinge state and calculated the topological phase diagram of our model. We found that the SOTI phase is stable up to relatively large values of the Zeeman field. The topological phase diagram also remains unaffected by external perturbations and disorder of strengths up to and even larger than the surface gap.

ACKNOWLEDGMENTS

We gratefully acknowledge many useful discussions with Silas Hoffman and Yanick Volpez. This work was supported by the Swiss National Science Foundation, NCCR QSIT, and the Georg H. Endress foundation. This project received funding from the European Union's Horizon 2020 research and innovation program (ERC Starting Grant, grant agreement No. 757725).

APPENDIX A: WAVE FUNCTIONS OF SURFACE STATES

In this Appendix, we calculate the wave functions of the states $|\Phi_{\pm}^s\rangle$ located at different surfaces s . We solve the Schrodinger equation obtained by making the substitution $k_j \rightarrow -i\partial_j$ with $j \in \{x, y, z\}$. For clarity, we only focus on the solutions at the Dirac point, which are obtained by taking two of three components of the momentum \mathbf{k} to zero. Then, by

adding perturbatively a small Zeeman field, we compute the gap opened in the spectrum of the edge states, see Sec. IV A.

1. Top and bottom surfaces

Solving the Schrodinger equation for $\mathcal{H}_{\text{TI}}^{\text{xy}}$ [see Eq. (7)] allows us to find two zero-energy solutions localized at the top surface at $z = 0$:

$$\begin{aligned} |\Phi_{\pm}^{\text{xy}}\rangle &= \frac{1}{\mathcal{N}} \sum_{\eta\tau\sigma} \int_{z=0}^{L_z} dz \Phi_{\pm\eta\tau\sigma}^{\text{xy}}(z) |z, \eta, \tau, \sigma\rangle, \\ \Phi_+^{\text{xy}}(z) &= e^{-z/\xi} (0, 0, 1, 0, 0, 0, -t_1/t_2, 0), \\ \Phi_-^{\text{xy}}(z) &= e^{-z/\xi} (0, 0, 0, -1, 0, 0, 0, t_1/t_2), \end{aligned} \quad (\text{A1})$$

where $\xi = t_1 t_2 \hbar a / (t_1^2 - t_2^2)$ and \mathcal{N} is a normalization constant. We recall that the wave function components are ordered as $(\Phi_{\pm 11\uparrow}^{\text{xy}}, \Phi_{\pm 11\downarrow}^{\text{xy}}, \Phi_{\pm 1\bar{1}\uparrow}^{\text{xy}}, \Phi_{\pm 1\bar{1}\downarrow}^{\text{xy}}, \Phi_{\pm \bar{1}1\uparrow}^{\text{xy}}, \Phi_{\pm \bar{1}1\downarrow}^{\text{xy}}, \Phi_{\pm \bar{1}\bar{1}\uparrow}^{\text{xy}}, \Phi_{\pm \bar{1}\bar{1}\downarrow}^{\text{xy}})$. The solutions satisfy the relations $T|\Phi_{\pm}^{\text{xy}}\rangle = \pm|\Phi_{\mp}^{\text{xy}}\rangle$ and $P|\Phi_{\pm}^{\text{xy}}\rangle = |\Phi_{\pm}^{\text{xy}}\rangle$. More generally, any combination of $|\Phi_+^{\text{xy}}\rangle$ and $|\Phi_-^{\text{xy}}\rangle$ (with its time-reversal partner) is also a solution of the problem, however, only these two states respect the rotational symmetry along the z spin axis present initially in \mathcal{H}_{TI} .

The dispersion relation and the effective Hamiltonian at small finite momentum k_{\parallel} is obtained perturbatively by calculating the expectation values of the remaining terms in \mathcal{H}_{TI} in the basis of the surface states $|\Phi_{\pm}^{\text{xy}}\rangle$ close to the Dirac point, assuming that the amplitude of the momentum k_{\parallel} is small. Hence, we only take into account the terms linear in k_x and k_y . We also distinguish between the diagonal and off-diagonal components of the expectation values. We find that all the diagonal components vanish exactly, i.e.,

$$\langle \Phi_{\pm}^{\text{xy}} | \alpha k_y \sigma_x \tau_z | \Phi_{\pm}^{\text{xy}} \rangle = \langle \Phi_{\pm}^{\text{xy}} | \alpha k_x \sigma_y \tau_z | \Phi_{\pm}^{\text{xy}} \rangle = 0. \quad (\text{A2})$$

However, the off-diagonal components are nonzero:

$$\begin{aligned} \langle \Phi_-^{\text{xy}} | \alpha k_y \sigma_x \tau_z | \Phi_+^{\text{xy}} \rangle &= \alpha k_y (t_1 - t_2) / \bar{t}, \\ \langle \Phi_-^{\text{xy}} | \alpha k_x \sigma_y \tau_z | \Phi_+^{\text{xy}} \rangle &= i \alpha k_x (t_1 - t_2) / \bar{t}, \\ \bar{t} &= 2\mathcal{N} \sqrt{t_2^2 + t_1^2} [\xi(1 - e^{-2L_z/\xi})]^{-1}. \end{aligned} \quad (\text{A3})$$

By using these results, the effective low-energy Hamiltonian density of the top xy surface in Eq. (8) can be derived.

The wave functions of the bottom xy surface at $z = L_z$ are obtained using the symmetry transformation $z \rightarrow L_z - z$, $e_j \rightarrow -e_j$, where e_j are three basis unit vectors. Under this transformation, the Hamiltonian density is modified as $\mathcal{H}_{\text{TI}}^{\text{xy}} \rightarrow \tau_x \mathcal{H}_{\text{TI}}^{\text{xy}} \tau_x$. Such a transformation preserves the orientation of the surface, so that the outward-pointing normal vector $\mathbf{v}_{\perp}^{\text{xy}}$ always coincides with the vector \mathbf{e}_z . As a result, we deduce that the wave functions of the states localized at $z = L_z$ read $\tau_x \Phi_{\pm}^{\text{xy}}(L_z - z)$. The effective low-energy Hamiltonian expressed in the basis of the surface states remains unaffected [see Eq. (9)].

2. Lateral surfaces

The zero-energy solutions of Eq. (10) describing the state localized at the $y = 0$ surface have the following general form:

$$\begin{aligned} |\Phi_{\pm}^{\text{xz}}\rangle &= \frac{1}{\mathcal{N}} \sum_{\sigma\eta\tau} \int dy \Phi_{\pm\eta\tau\sigma}^{\text{xz}}(y) |y, \eta, \tau, \sigma\rangle, \\ \Phi_+^{\text{xz}}(y) &= \sum_j C_j e^{-y/\xi_j} e^{iq_j y} \Phi_{+j}^{\text{xz}}(y), \\ \Phi_-^{\text{xz}}(y) &= \sum_j C_j^* e^{-y/\xi_j} e^{-iq_j y} \Phi_{-j}^{\text{xz}}(y), \end{aligned} \quad (\text{A4})$$

where C_j are complex coefficients and $\Phi_{\pm j}^{\text{xz}}(y)$ are wave functions satisfying $T\Phi_{\pm j}^{\text{xz}} = \pm\Phi_{\mp j}^{\text{xz}}$, $P\Phi_{\pm j}^{\text{xz}} = \Phi_{\pm j}^{\text{xz}}$, and $\sigma_x \Phi_{\mu j}^{\text{xz}} = \pm\Phi_{\mu j}^{\text{xz}}$. Each wave function $\Phi_{\pm j}^{\text{xz}}$ is associated with a decay length ξ_j and a wave vector q_j , which can be calculated as $\xi_j = 1/\Re(\lambda_j)$ and $q_j = \Im(\lambda_j)$ [58], where λ_j are solutions of

$$\begin{aligned} \left(\frac{\hbar^2}{2m}\right)^4 \lambda^8 + 2\left(\frac{\hbar^2}{2m}\right) \alpha^2 \lambda^6 + \left[\alpha^4 + \left(\frac{\hbar^2}{2m}\right)^2 (t_1^2 + t_2^2)\right] \lambda^4 \\ - 2\alpha^2 (t_1^2 + t_2^2) \lambda^2 + (t_1^2 - t_2^2)^2 - 4t_1^2 \left(\frac{\hbar^2}{2m}\right)^2 = 0. \end{aligned} \quad (\text{A5})$$

Solutions of the above equation can be obtained analytically. For the sake of readability, we do not provide an exact expression here. However, we point out an important difference with respect to the lateral surface case. The solutions of Eq. (A5) are, in general, complex such that both ξ_j and q_j are nonzero. This corresponds to an exponentially decaying solution which oscillates, in contrast to the surface states on the top and bottom surfaces which are simply decaying. Due to the high complexity of the problem, we do not provide an analytical expression of the wave functions $\Phi_{\pm j}^{\text{xz}}$ and the coefficients C_j . Nevertheless, we are able to solve the one-dimensional problem associated with Eq. (10) numerically. This allows us to estimate the expectation values of the remaining terms in \mathcal{H}_{TI} in the basis of $|\Phi_{\pm}^{\text{xz}}\rangle$. In general, we find that the diagonal components, as well as the real and the imaginary part of the off-diagonal components, are nonzero for all the terms, as a result of the strong anisotropy between the x and z directions. However, we find that one of the contributions is usually by an order of magnitude larger than the other terms. Below, we express the diagonal components of the expectation values that accounts for this largest contribution,

$$\begin{aligned} \langle \Phi_{\pm}^{\text{xz}} | \alpha k_x \sigma_y \tau_z | \Phi_{\pm}^{\text{xz}} \rangle &= \pm \alpha A k_x, \quad A \in \mathbb{R}, \\ \langle \Phi_{\pm}^{\text{xz}} | t_1 k_z a (\eta_0 - \eta_z) \tau_y | \Phi_{\pm}^{\text{xz}} \rangle &= 0. \end{aligned} \quad (\text{A6})$$

Here, A is a coefficient that depends on the parameters of the system and the constants C_j . Similarly, we calculate the off-diagonal components

$$\begin{aligned} \langle \Phi_-^{\text{xz}} | \alpha k_x \sigma_y \tau_z | \Phi_+^{\text{xz}} \rangle &= 0, \\ \langle \Phi_-^{\text{xz}} | t_1 k_z a (\eta_0 - \eta_z) \tau_y | \Phi_+^{\text{xz}} \rangle &= t_1 B k_z a, \quad B \in \mathbb{R}. \end{aligned} \quad (\text{A7})$$

As a consequence, we obtain the effective low-energy Hamiltonian of the surface states at $y = 0$ in Eq. (11). The wave functions of the lateral surface at $y = L_y$ are obtained by using the transformation $y \rightarrow L_y - y$, $e_j \rightarrow -e_j$, which preserves

the surface orientation such that the normal vector \mathbf{v}_\perp^{xz} pointing outward from the surface coincides with the vector \mathbf{e}_y . Under this transformation, the Hamiltonian density transforms as $\mathcal{H}_{\text{TI}}^{xz} \rightarrow \sigma_y \mathcal{H}_{\text{TI}}^{xz} \sigma_y$, which allows us to express the surface state wave functions as $\sigma_y \Phi_\pm^{xz}(L_y - y)$.

Finally, the wave functions of the two remaining yz surfaces can be obtained by using the rotational symmetry in the xy plane described by the transformation $\{L_x - x, y\} \rightarrow \{y, x\}$. Using this symmetry allows us to express the wave functions of the surface states localized at the yz surfaces at $x = 0$ as $i\sigma_z \Phi_\pm^{xz}(x)$. Similarly, we find that the wave functions of the surface states localized at $x = L_x$ are $\sigma_x \Phi_\pm^{xz}(L_x - x)$.

3. Projections of the staggered Zeeman field

Using the expression of the wave functions $\Phi_\pm^{xy}(z)$ of the surface states located on the top xy surface at $z = 0$, we calculate the expectation values of the Zeeman term \mathcal{H}_Z in the neighborhood of the Dirac point. We obtain the following diagonal contributions:

$$\begin{aligned} \langle \Phi_\pm^{xy} | t_Z n_x \sigma_x \eta_z | \Phi_\pm^{xy} \rangle &= \langle \Phi_\pm^{xy} | t_Z n_y \sigma_y \eta_z | \Phi_\pm^{xy} \rangle = 0, \\ \langle \Phi_\pm^{xy} | t_Z n_z \sigma_z \eta_z | \Phi_\pm^{xy} \rangle &= \pm t_Z n_z (t_1 + t_2) / \bar{t}. \end{aligned} \quad (\text{A8})$$

Similarly, we calculate the off-diagonal contributions

$$\begin{aligned} \langle \Phi_-^{xy} | t_Z n_x \sigma_x \eta_z | \Phi_+^{xy} \rangle &= -t_Z n_x (t_1 + t_2) / \bar{t}, \\ \langle \Phi_-^{xy} | t_Z n_y \sigma_y \eta_z | \Phi_+^{xy} \rangle &= -it_Z n_y (t_1 + t_2) / \bar{t}, \\ \langle \Phi_-^{xy} | t_Z n_z \sigma_z \eta_z | \Phi_+^{xy} \rangle &= 0. \end{aligned} \quad (\text{A9})$$

Using these results, we obtained the effective low-energy Hamiltonian density describing the top xy surface of the 3DTI under the applied Zeeman field in Eqs. (15) and (16).

Next, we perform the calculations for the bottom xy surface at $z = L_z$. We note that the projection of the Zeeman field vector \mathbf{n} onto the normal unit vector \mathbf{v}_\perp^{xy} , pointing outwards of the surface, changes sign. In other words, applying the surface-interchanging transformation from Appendix A 1 results in the inversion of the direction of the Zeeman field $\mathbf{n} \rightarrow -\mathbf{n}$. Using the results of Appendix A 2, we analyze the effect of the Zeeman field on the surface states localized on the lateral xz surfaces at $y = 0$. Below we provide the result of a numerical calculation of the expectation value of the Zeeman term \mathcal{H}_Z in the basis of states $|\Phi_\pm^{xz}\rangle$. For the diagonal components of the expectation values, we obtain

$$\begin{aligned} \langle \Phi_\pm^{xz} | t_Z n_x \sigma_x \eta_z | \Phi_\pm^{xz} \rangle &= \langle \Phi_\pm^{xz} | t_Z n_y \sigma_y \eta_z | \Phi_\pm^{xz} \rangle = 0, \\ \langle \Phi_\pm^{xz} | t_Z n_z \sigma_z \eta_z | \Phi_\pm^{xz} \rangle &= \pm t_Z n_z C, \quad C \in \mathbb{R}. \end{aligned} \quad (\text{A10})$$

Similarly, for the off-diagonal components, we find

$$\begin{aligned} \langle \Phi_-^{xz} | t_Z n_x \sigma_x \eta_z | \Phi_+^{xz} \rangle &= \langle \Phi_-^{xz} | t_Z n_z \sigma_z \eta_z | \Phi_+^{xz} \rangle = 0, \\ \langle \Phi_-^{xz} | t_Z n_y \sigma_y \eta_z | \Phi_+^{xz} \rangle &= it_Z n_y C. \end{aligned} \quad (\text{A11})$$

This allows us to obtain the effective low-energy Hamiltonian of the $y = 0$ surface in Eq. (19). In order to describe the low-energy physics of the $y = L_y$ surface and obtain Eq. (20), we use the transformation $y \rightarrow L_y - y$, $\mathbf{e}_j \rightarrow -\mathbf{e}_j$, which preserves the orientation of the lateral surface and changes the direction of the Zeeman field.

APPENDIX B: EFFECT OF THE UNIFORM ZEEMAN FIELD

In the main text, we found that the staggered Zeeman field, described by the term

$$\mathcal{H}_Z = t_Z \mathbf{n} \cdot \boldsymbol{\sigma} \eta_z, \quad (\text{B1})$$

opens a gap in the spectrum of gapless surface states of a 3DTI, associated with mass term of amplitude M_s . The mass M_s changes sign between opposite faces, leading to the emergence of gapless hinge states. In this Appendix, we show that the uniform magnetic field described by a Zeeman term

$$\mathcal{H}_{ZU} = t_Z \mathbf{n} \cdot \boldsymbol{\sigma} \quad (\text{B2})$$

fails to open a gap in the spectrum of gapless surface states, and does not allow one to generate hinge states.

1. Top and bottom surfaces

First, we focus on the top xy surface and the surface states $\Phi_\pm^{xy}(z)$ localized at $z = 0$. We calculate the expectation values of the Zeeman term \mathcal{H}_{ZU} in the neighborhood of the Dirac point. We obtain the following diagonal contributions:

$$\begin{aligned} \langle \Phi_\pm^{xy} | t_Z n_x \sigma_x | \Phi_\pm^{xy} \rangle &= \langle \Phi_\pm^{xy} | t_Z n_y \sigma_y | \Phi_\pm^{xy} \rangle = 0, \\ \langle \Phi_\pm^{xy} | t_Z n_z \sigma_z | \Phi_\pm^{xy} \rangle &= \pm t_Z n_z (t_1 - t_2) / \bar{t}. \end{aligned} \quad (\text{B3})$$

Similarly, we calculate the off-diagonal contributions

$$\begin{aligned} \langle \Phi_-^{xy} | t_Z n_x \sigma_x | \Phi_+^{xy} \rangle &= -t_Z n_x (t_1 - t_2) / \bar{t}, \\ \langle \Phi_-^{xy} | t_Z n_y \sigma_y | \Phi_+^{xy} \rangle &= -it_Z n_y (t_1 - t_2) / \bar{t}, \\ \langle \Phi_-^{xy} | t_Z n_z \sigma_z | \Phi_+^{xy} \rangle &= 0. \end{aligned} \quad (\text{B4})$$

This allows us to write the effective low-energy Hamiltonian density as follows:

$$\begin{aligned} \mathcal{H}_{\text{SOTI}}^{xy}(z=0) &\approx \alpha(\rho_x k_y - \rho_y k_x)(t_1 - t_2) / \bar{t} \\ &\quad - t_Z(n_x \rho_x + n_y \rho_y - n_z \rho_z)(t_1 - t_2) / \bar{t}. \end{aligned} \quad (\text{B5})$$

We see that, similarly to the staggered Zeeman field, the x and y components of the uniform Zeeman field simply shift the position of the Dirac cone in momentum space, while the z component gaps out the surface states $|\Phi_\pm^{xy}\rangle$. We note, however, that the amplitude of the mass term generated by the uniform field is changed: $M_{xy} = t_Z n_z (t_1 - t_2) / \bar{t}$. Our analytical predictions are confirmed by numerical calculations shown in Fig. 6(a).

2. Lateral surfaces

Second, using the results of Sec. III B 2, we calculate the effect of the uniform Zeeman field on the surface states localized on the lateral xz surface at $y = 0$. A numerical calculation of the diagonal components of the expectation values provides the following result:

$$\begin{aligned} \langle \Phi_\pm^{xz} | t_Z n_x \sigma_x | \Phi_\pm^{xz} \rangle &= \langle \Phi_\pm^{xz} | t_Z n_y \sigma_y | \Phi_\pm^{xz} \rangle \\ &= \langle \Phi_\pm^{xz} | t_Z n_z \sigma_z | \Phi_\pm^{xz} \rangle = 0. \end{aligned} \quad (\text{B6})$$

Similarly, for the off-diagonal components, we find

$$\begin{aligned} \langle \Phi_-^{xz} | t_Z n_y \sigma_y | \Phi_+^{xz} \rangle &= \langle \Phi_-^{xz} | t_Z n_z \sigma_z | \Phi_+^{xz} \rangle = 0, \\ \langle \Phi_-^{xz} | t_Z n_x \sigma_x | \Phi_+^{xz} \rangle &= t_Z n_x C. \end{aligned} \quad (\text{B7})$$

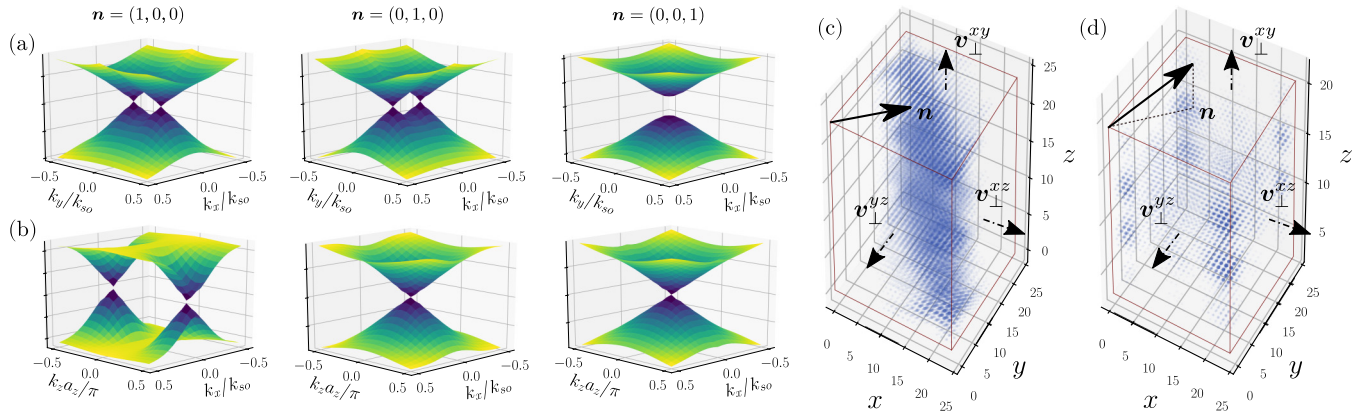


FIG. 6. [(a) and (b)] The effect of the uniform Zeeman field on the dispersion relation of the surface states (a) $|\Phi_{\pm}^{xy}\rangle$ and (b) $|\Phi_{\pm}^{xz}\rangle$. The direction of the Zeeman field is indicated by the vector \mathbf{n} . The z component of the Zeeman field gaps out the surface states at the top and bottom surfaces. The surface states at the lateral surfaces stay gapless for all the directions of the Zeeman field. Parameters of the simulations are $t_1 = 2t_2 = E_{s0}$, $t_z = 0.3E_{s0}$. [(c) and (d)] Probability density of the state closest to the chemical potential, obtained in numerical simulations with OBCs along the x , y , and z directions. The black arrows indicate the direction of the Zeeman field. (c) If $\mathbf{n} = (1, 1, 0)/\sqrt{2}$, the Zeeman field fails to open a gap on any surface. (d) The Zeeman field with $\mathbf{n} = (1, 1, 1)/\sqrt{3}$ gaps out the xy surfaces but leaves the lateral surfaces gapped. Parameters of the simulations are $t_1 = 2t_2 = 4E_{s0}$ and $t_z = 2E_{s0}$.

This allows us to write down the effective low-energy Hamiltonian of the $y = 0$ surface

$$\mathcal{H}_{\text{SOTI}}^{xz}(y=0) \approx \alpha A k_x \rho_z + t_1 B k_z a \rho_x + t_z C n_x \rho_x. \quad (\text{B8})$$

Surprisingly, we find that the only component of the Zeeman field that affects the low-energy degrees of freedom is the x component. Its main effect consists in shifting the Dirac cone along the k_z axis in momentum space. We confirm these analytical predictions using numerical simulations, shown in Fig. 6(b). We see that the gap remains closed for any direction of the Zeeman field. We also note that the momentum shift originating from the uniform Zeeman field is much larger than the one originating from the staggered field.

3. Numerical confirmation

As a final confirmation of the effect of the uniform Zeeman field, we perform numerical simulations of the system in a geometry with OBC along all the three axis directions. The results of such simulations are shown in Figs. 3(c) and 3(d). Similar to the calculation in the main text, we consider two different geometries: with the Zeeman field parallel to the xy surface and with the Zeeman field making a finite angle with all the three surfaces. As expected from our theoretical analysis, the z component of the uniform Zeeman field gaps out the surfaces states localized at the top and bottom surfaces. No components of the Zeeman field open a gap for the surface states localized at the lateral surfaces.

APPENDIX C: TOPOLOGICAL INVARIANTS

1. 3DTI phase

In the absence of a Zeeman field, the system of coupled Rashba 2DEG layers is characterized by the topological phase diagram consisting of two distinct topological phases: the trivial insulating phase for $t_1 < t_2$ and the strong 3DTI for $t_1 > t_2$. This topological description relies on the $\nu_0 \in \mathbb{Z}_2$ topological invariant, which counts the parity of the number of Dirac

cones in the surface state dispersion relation. The invariant ν_0 is an appropriate choice for the AII symmetry class to which our setup belongs to. In this section, we make also use of the additional inversion symmetry $I = \tau_x$, verifying $I\mathcal{H}_{\text{TI}}(\mathbf{k})I^{-1} = \mathcal{H}_{\text{TI}}(-\mathbf{k})$ and express the topological invariant ν_0 using the approach proposed in Ref. [59]. We note that I is present only in the clean limit, however, the topological phases we consider below are stable against potential disorder and do not require the inversion symmetry. However, the theoretical calculations are substantially simpler if one can rely on I .

First, following Ref. [59], we calculate the inversion parity eigenvalues $\zeta_{2j}(\mathbf{Q}_i) = \pm 1$, $j = 1, \dots, n_{\text{occ}}/2$ of the n_{occ} occupied energy bands at the high-symmetry points \mathbf{Q}_i (i.e., momenta inside the first Brillouin zone, which are mapped onto themselves by the inversion). Due to the Kramers theorem, n_{occ} is necessarily an even number ($n_{\text{occ}} = 4$ in our case) and the states $2j$ and $2j - 1$ share the same eigenvalues at \mathbf{Q}_i . Hence, we take into account only one such eigenvalue per each Kramers pair. The resulting \mathbb{Z}_2 topological invariant can be expressed as

$$(-1)^{\nu_0} = \prod_i \prod_{j=1}^{n_{\text{occ}}/2} \zeta_{2j}(\mathbf{Q}_i). \quad (\text{C1})$$

The result of the numerical calculation of the \mathbb{Z}_2 topological invariant in our model is shown in Fig. 7(a). The trivial phase ($t_1 < t_2$) is associated with the topological invariant $\nu_0 = 0$, while the strong 3DTI phase ($t_1 > t_2$) is associated with $\nu_0 = 1$ corresponding to the presence of one single unpaired Dirac cone on the system surface. This result is in agreement with our analytical findings in the main part, see the phase diagram at $t_z = 0$ shown in Fig. 4(a).

2. HOTI phase

In this part, we compute the topological invariant that distinguishes between the HOTI and the trivial phases

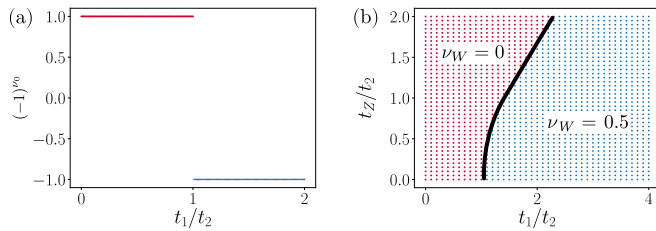


FIG. 7. (a) The topological phase diagram calculated numerically using the \mathbb{Z}_2 -topological invariant ν_0 as a function of the ratio t_1/t_2 for $t_2 = 0.5E_{so}$ in the absence of magnetic fields, $t_z = 0$. The 3DTI phase (represented by blue dots) is characterized by a topological invariant $\nu_0 = 1$, while the trivial phase (represented by red dots) is characterized by $\nu_0 = 0$. The results are in full agreement with the phase diagram at $t_z = 0$ from Fig. 4(a). (b) The topological phase diagram calculated using the Wannier function topological invariant as a function of the ratios t_1/t_2 and t_z/t_2 for $t_2 = 0.5E_{so}$. The SOTI phase (represented by blue dots) is characterized by a topological invariant $\nu_W = 0.5$, while the trivial phase (represented by red dots) is characterized by $\nu_W = 0$. The black line separates the two phases and marks a topological phase transition. The position of this topological phase transition line is not affected by the direction of the Zeeman field.

appearing in the phase diagram of Fig. 4(a). For this purpose, we employ a method based on symmetry-adapted Wannier functions [60,61]. In the presence of the staggered magnetic field, the only remaining symmetry in our system is the inversion symmetry $I = \tau_x$. We define the Wannier functions for a three-dimensional inversion-symmetric system as $w_{\zeta,j}(\mathbf{x})$, where $\zeta = \pm 1$ is the corresponding eigenvalue of the inversion symmetry operator, $j = 1, \dots, n_{occ}$ is the band index, and n_{occ} is the total number of occupied bands. In the following, we are interested only in Wannier functions localized at inversion-symmetric invariant positions (i.e., positions inside the unit cell which are mapped onto themselves by the inversion) $\{\mathbf{W}_1, \dots, \mathbf{W}_8\}$, known as Wyckoff positions. Let us introduce the numbers of occupied Wannier orbitals localized at Wyckoff positions $\nu_{W_i,\zeta,j}$, which can assume only the values 0 or 1. Based on these quantities, we can introduce the following topological invariants:

$$\nu_{W_i} = \sum_{j=1}^{n_{occ}} (\nu_{W_i,-,j} - \nu_{W_i,+,j}), \quad i = 1, \dots, 8, \quad (\text{C2})$$

where the sum runs over all occupied bands. These topological invariants correspond to the difference between odd and even

Wannier orbitals centered at each Wyckoff position. This set of quantities is used to discriminate between topological and trivial phases. In particular, a phase is classified as topologically nontrivial when all these topological invariants are non-integer, namely, $\nu_{W_i} \notin \mathbb{Z}$ for all i . When this condition is false, namely, $\nu_{W_i} \in \mathbb{Z}$ for some i , the phase is topologically trivial.

In order to numerically compute these real-space invariants, it is convenient to relate them to invariants defined in momentum space. To this end, a link can be found between the quantities in Eq. (C2) and the symmetry indicators of band structure $n_{\zeta,j}(\mathbf{Q}_i)$, which correspond to the number of even ($\zeta = 1$) and odd ($\zeta = -1$) eigenvalues of the inversion operator computed for all invariant momenta \mathbf{Q}_i [60]. The mapping is given by

$$\begin{pmatrix} \nu_{W_1} \\ \nu_{W_2} \\ \nu_{W_3} \\ \nu_{W_4} \\ \nu_{W_5} \\ \nu_{W_6} \\ \nu_{W_7} \\ \nu_{W_8} \end{pmatrix} = \sum_{j=1}^{n_{occ}} A \cdot \begin{pmatrix} n_{-,j}(\mathbf{Q}_1) - n_{+,j}(\mathbf{Q}_1) \\ n_{-,j}(\mathbf{Q}_2) - n_{+,j}(\mathbf{Q}_2) \\ n_{-,j}(\mathbf{Q}_3) - n_{+,j}(\mathbf{Q}_3) \\ n_{-,j}(\mathbf{Q}_4) - n_{+,j}(\mathbf{Q}_4) \\ n_{-,j}(\mathbf{Q}_5) - n_{+,j}(\mathbf{Q}_5) \\ n_{-,j}(\mathbf{Q}_6) - n_{+,j}(\mathbf{Q}_6) \\ n_{-,j}(\mathbf{Q}_7) - n_{+,j}(\mathbf{Q}_7) \\ n_{-,j}(\mathbf{Q}_8) - n_{+,j}(\mathbf{Q}_8) \end{pmatrix}, \quad (\text{C3})$$

where the sum is extended over all occupied bands and A is a 8×8 matrix whose elements are given by $A_{ij} = \exp(i\mathbf{Q}_i \cdot \mathbf{W}_j)/8$. We comment here that, according to Eq. (C3), ν_{W_i} are true topological invariants, since inversion-symmetry eigenvalues can be modified only by closing and reopening of the gap.

In our case, we find that all real-space topological invariants are all the same and that the topology of the phase is determined by a single invariant ν_W ,

$$\nu_W \equiv \nu_{W_1} = \dots = \nu_{W_8}. \quad (\text{C4})$$

In Fig. 7(b), we present the topological phase diagram as a function of t_1/t_2 and t_z/t_2 . According to the topological criterion outlined above, the phase characterized by $\nu_W = 0$ is topologically trivial, while the phase with $\nu_W = 0.5$ is a stable topological phase. This topological phase diagram is in full agreement with the phase diagram presented in Fig. 4(a) in which the topological boundaries between different phases were obtained by computing the gap to the first excited state.

[1] M. Z. Hasan and C. L. Kane, *Rev. Mod. Phys.* **82**, 3045 (2010).
 [2] X.-L. Qi and S.-C. Zhang, *Rev. Mod. Phys.* **83**, 1057 (2011).
 [3] M. Sato and Y. Ando, *Rep. Prog. Phys.* **80**, 076501 (2017).
 [4] J. Wang and S.-C. Zhang, *Nat. Mater.* **16**, 1062 (2017).
 [5] X.-G. Wen, *Rev. Mod. Phys.* **89**, 41004 (2017).
 [6] M. H. Freedman, A. Kitaev, M. J. Larsen, and Z. Wang, *Bull. Amer. Math. Soc.* **40**, 31 (2003).
 [7] A. Kitaev, *Ann. Phys.* **303**, 2 (2003).

[8] A. Stern and N. H. Lindner, *Science* **339**, 1179 (2013).
 [9] R.-J. Slager, L. Rademaker, J. Zaanen, and L. Balents, *Phys. Rev. B* **92**, 085126 (2015).
 [10] W. A. Benalcazar, B. A. Bernevig, and T. L. Hughes, *Science* **357**, 61 (2017).
 [11] W. A. Benalcazar, B. A. Bernevig, and T. L. Hughes, *Phys. Rev. B* **96**, 245115 (2017).
 [12] Z. Song, Z. Fang, and C. Fang, *Phys. Rev. Lett.* **119**, 246402 (2017).

- [13] J. Langbehn, Y. Peng, L. Trifunovic, F. von Oppen, and P. W. Brouwer, *Phys. Rev. Lett.* **119**, 246401 (2017).
- [14] Y. Peng, Y. Bao, and F. von Oppen, *Phys. Rev. B* **95**, 235143 (2017).
- [15] M. Geier, L. Trifunovic, M. Hoskam, and P. W. Brouwer, *Phys. Rev. B* **97**, 205135 (2018).
- [16] E. Khalaf, *Phys. Rev. B* **97**, 205136 (2018).
- [17] C.-H. Hsu, P. Stano, J. Klinovaja, and D. Loss, *Phys. Rev. Lett.* **121**, 196801 (2018).
- [18] T. Liu, J. J. He, and F. Nori, *Phys. Rev. B* **98**, 245413 (2018).
- [19] Z. Yan, F. Song, and Z. Wang, *Phys. Rev. Lett.* **121**, 096803 (2018).
- [20] Y. Volpez, D. Loss, and J. Klinovaja, *Phys. Rev. Lett.* **122**, 126402 (2019).
- [21] M. Ezawa, *Sci. Rep.* **9**, 5286 (2019).
- [22] D. Calugaru, V. Juricic, and B. Roy, *Phys. Rev. B* **99**, 041301(R) (2019).
- [23] A. Agarwala, V. Juricic, and B. Roy, [arXiv:1902.00507](https://arxiv.org/abs/1902.00507).
- [24] K. Laubscher, D. Loss, and J. Klinovaja, *Phys. Rev. Research* **1**, 032017 (2019).
- [25] Z. Yan, *Phys. Rev. Lett.* **123**, 177001 (2019).
- [26] K. Plekhanov, M. Thakurathi, D. Loss, and J. Klinovaja, *Phys. Rev. Research* **1**, 032013 (2019).
- [27] S. Franca, D. V. Efremov, and I. C. Fulga, *Phys. Rev. B* **100**, 075415 (2019).
- [28] R.-X. Zhang, W. S. Cole, and S. Das Sarma, *Phys. Rev. Lett.* **122**, 187001 (2019).
- [29] S.-B. Zhang and B. Trauzettel, *Phys. Rev. Research* **2**, 012018 (2020).
- [30] S. H. Kooi, G. van Miert, and C. Ortix, *Phys. Rev. B* **98**, 245102 (2018).
- [31] S. H. Kooi, G. van Miert, and C. Ortix, [arXiv:1908.00879](https://arxiv.org/abs/1908.00879).
- [32] Y. Tanaka, R. Takahashi, and S. Murakami, [arXiv:1910.05938](https://arxiv.org/abs/1910.05938).
- [33] Y. Tanaka, R. Takahashi, and S. Murakami, [arXiv:1910.08290](https://arxiv.org/abs/1910.08290).
- [34] C. W. Peterson, W. A. Benalcazar, T. L. Hughes, and G. Bahl, *Nature (London)* **555**, 346 (2018).
- [35] S. Imhof, C. Berger, F. Bayer, J. Brehm, L. W. Molenkamp, T. Kiessling, F. Schindler, C. H. Lee, M. Greiter, T. Neupert, and R. Thomale, *Nat. Phys.* **14**, 925 (2018).
- [36] S. Mittal, V. V. Orre, G. Zhu, M. A. Gorlach, A. Poddubny, and M. Hafezi, *Nat. Photonics* **13**, 692 (2019).
- [37] X.-D. Chen, W.-M. Deng, F.-L. Shi, F.-L. Zhao, M. Chen, and J.-W. Dong, *Phys. Rev. Lett.* **122**, 233902 (2019).
- [38] A. E. Hassan, F. K. Kunst, A. Moritz, G. Andler, E. J. Bergholtz, and M. Bourennane, *Nat. Photonics* **13**, 697 (2019).
- [39] M. Serra-Garcia, V. Peri, R. Süssstrunk, O. R. Bilal, T. Larsen, L. G. Villanueva, and S. D. Huber, *Nature (London)* **555**, 342 (2018).
- [40] H. Xue, Y. Yang, F. Gao, Y. Chong, and B. Zhang, *Nat. Mater.* **18**, 108 (2019).
- [41] F. Schindler, A. M. Cook, M. G. Vergniory, Z. Wang, S. S. P. Parkin, B. A. Bernevig, and T. Neupert, *Sci. Adv.* **4**, eaat0346 (2018).
- [42] F. Schindler, Z. Wang, M. G. Vergniory, A. M. Cook, A. Murani, S. Sengupta, A. Y. Kasumov, R. Deblock, S. Jeon, I. Drozdov, H. Bouchiat, S. Guéron, A. Yazdani, B. A. Bernevig, and T. Neupert, *Nat. Phys.* **14**, 918 (2018).
- [43] X. Ni, M. Weiner, A. Alú, and A. B. Khanikaev, *Nat. Mater.* **18**, 113 (2019).
- [44] X. Zhang, B.-Y. Xie, H.-F. Wang, X. Xu, Y. Tian, J.-H. Jiang, M.-H. Lu, and Y.-F. Chen, *Nat. Commun.* **10**, 5331 (2019).
- [45] L. Trifunovic, D. Loss, and J. Klinovaja, *Phys. Rev. B* **93**, 205406 (2016).
- [46] Y. Volpez, D. Loss, and J. Klinovaja, *Phys. Rev. B* **96**, 085422 (2017).
- [47] Q. Liu, C.-X. Liu, C. Xu, X.-L. Qi, and S.-C. Zhang, *Phys. Rev. Lett.* **102**, 156603 (2009).
- [48] Y. L. Chen, J.-H. Chu, J. G. Analytis, Z. K. Liu, K. Igarashi, H.-H. Kuo, X. L. Qi, S. K. Mo, R. G. Moore, D. H. Lu, M. Hashimoto, T. Sasagawa, S. C. Zhang, I. R. Fisher, Z. Hussain, and Z. X. Shen, *Science* **329**, 659 (2010).
- [49] A. A. Burkov and L. Balents, *Phys. Rev. Lett.* **107**, 127205 (2011).
- [50] C. H. Hsu, P. Stano, J. Klinovaja, and D. Loss, *Phys. Rev. B* **96**, 081405(R) (2017).
- [51] M. M. Desjardins, L. C. Contamin, M. R. Delbecq, M. C. Dartiailh, L. E. Bruhat, T. Cubaynes, J. J. Viennot, F. Mallet, S. Rohart, A. Thiaville, A. Cottet, and T. Kontos, *Nat. Mater.* **18**, 1060 (2019).
- [52] F. Ma, W. Ji, J. Hu, Z.-Y. Lu, and T. Xiang, *Phys. Rev. Lett.* **102**, 177003 (2009).
- [53] M. Enayat, Z. Sun, U. R. Singh, R. Aluru, S. Schmaus, A. Yaresko, Y. Liu, C. Lin, V. Tsurkan, A. Loidl, J. Deisenhofer, and P. Wahl, *Science* **345**, 653 (2014).
- [54] S. Manna, A. Kamalpure, L. Cornils, T. Hanke, E. M. J. Hedegaard, M. Bremholm, B. B. Iversen, Ph. Hofmann, J. Wiebe, and R. Wiesendanger, *Nat. Commun.* **8**, 14074 (2017).
- [55] D. Hsieh, Y. Xia, L. Wray, D. Qian, A. Pal, J. H. Dil, J. Osterwalder, F. Meier, G. Bihlmayer, C. L. Kane, Y. S. Hor, R. J. Cava, and M. Z. Hasan, *Science* **323**, 919 (2009).
- [56] Y. L. Chen, J. G. Analytis, J.-H. Chu, Z. K. Liu, S.-K. Mo, X. L. Qi, H. J. Zhang, D. H. Lu, X. Dai, Z. Fang, S. C. Zhang, I. R. Fisher, Z. Hussain, and Z.-X. Shen, *Science* **325**, 178 (2009).
- [57] K. Kuroda, M. Ye, A. Kimura, S. V. Ereemeev, E. E. Krasovskii, E. V. Chulkov, Y. Ueda, K. Miyamoto, T. Okuda, K. Shimada, H. Namatame, and M. Taniguchi, *Phys. Rev. Lett.* **105**, 146801 (2010).
- [58] J. Klinovaja and D. Loss, *Phys. Rev. B* **86**, 085408 (2012).
- [59] L. Fu and C. L. Kane, *Phys. Rev. B* **76**, 045302 (2007).
- [60] G. van Miert and C. Ortix, *Phys. Rev. B* **98**, 081110(R) (2018).
- [61] Y. Hwang, J. Ahn, and B.-J. Yang, *Phys. Rev. B* **100**, 205126 (2019).